

Rayleigh-wave H/V ratio measurement from ambient noise cross-correlations and its sensitivity to V_P : a numerical study

Ajay Malkoti^{†*}, Arjun Datta^{††} and Shravan M. Hanasoge

Department of Astronomy and Astrophysics, Tata Institute of Fundamental Research, Homi Bhabha Road, Colaba, Mumbai 400005, India. E-mail: arjundatta@iiserpune.ac.in

Accepted 2021 June 5. Received 2021 June 3; in original form 2020 September 24

SUMMARY

The promise of passive seismology has increasingly been realized in recent years. Given the expense in installing and maintaining seismic station networks, it is important to extract as much information from the measurements as possible. In this context, the ellipticity or H/V amplitude ratio of Rayleigh waves can prove to be a valuable observable in ambient noise seismology due to its complimentary sensitivity to subsurface structure, compared to phase and group-velocity dispersion, as well as its potential for constraining V_P structure in addition to V_S . However, the suitability of the Rayleigh H/V ratio in noise-based studies depends on the accurate interpretation of measurements made on multicomponent ambient-noise cross-correlations. We present a synthetic study that critically examines measurements commonly interpreted as the Rayleigh-wave H/V ratio, under realistic scenarios of spatially distributed and non-uniform noise sources. Using the surface wave terms of Green's function in a laterally homogeneous medium, we rigorously model multicomponent cross-correlations for arbitrary noise-source distributions and extract from them standard estimates of the H/V ratio. Variation of these measurements as a function of V_P is studied empirically, by brute-force simulation. We find that the measurements depart significantly from the theoretical Rayleigh-wave H/V for the medium in question, when noise sources are strongly directional or anisotropic. Love waves, if present in the cross-correlations, also have the potential to significantly bias interpretation. Accurate interpretation of the H/V ratio measurement thus rests on carefully modelling these effects. However, the sensitivity to V_P structure is comparable to that of the classic Rayleigh-wave H/V . We also propose a new measurement for cross-correlations that has slightly greater sensitivity to V_P . Finally, uncertainty analysis on synthetic tests suggests that simplistic interpretations of Rayleigh-wave ellipticity are only effective (in resolving V_P structure) when the Love-wave contamination is negligible and measurement uncertainties are less than 10 per cent.

Key words: Crustal imaging; Seismic interferometry; Seismic noise; Surface waves and free oscillations.

1 INTRODUCTION

Ambient noise cross-correlation is a popular technique used to study shallow Earth structure using observations of the ambient seismic field on Earth, commonly known as ‘ambient noise’. The widespread use of this technique over the last 15 yr has been largely

based on the theoretical principle that the cross-correlation of a diffuse and equipartitioned noise wavefield recorded at two receivers, is proportional to the causal and anticausal far-field Green's function between them (Shapiro & Campillo 2004; Snieder 2004; Weaver & Lobkis 2004). Heavy pre-processing of raw noise records and averaging of cross-correlations over sufficiently long times is adopted in practice (Bensen *et al.* 2007), to recover ‘empirical Green's functions’. Even so, most applications recover only the surface wave Green's function because the global noise field is dominated by ocean microseisms (Ardhuin *et al.* 2011, 2015) which originate near the Earth's surface and strongly excite seismic surface waves. Since the traditional surface wave measurements of phase and group velocity dispersion are dominantly sensitive to shear wave velocity

*Now at: CSIR-National Geophysical Research Institute, Hyderabad 500007, India

†Now at: Department of Earth and Climate Science, Indian Institute of Science Education and Research Pune, Dr. Homi Bhabha Road, Pashan, Pune 411008, India

(V_S), ambient noise has primarily been used to study Earth's V_S structure.

By contrast, recovery of P -wave velocities (V_P) from ambient noise is more challenging. Body waves, including P -waves, are hard to detect in ambient noise cross-correlations (due to weak excitation by shallow sources producing the noise wavefield) and the number of studies that have succeeded in doing so are limited (e.g. Roux *et al.* 2005; Poli *et al.* 2012; Nakata *et al.* 2015, 2016; Liu *et al.* 2016; Saygin *et al.* 2017; Pedersen & Colombi 2018; Wang *et al.* 2018). An alternative candidate approach for studying V_P , which does not require P -wave observations, is to make use of the Rayleigh-wave ellipticity or H/V ratio.

Rayleigh-wave H/V ratio (ratio of horizontal to vertical component amplitudes) is an unconventional surface wave observable compared to the more widely used dispersion measurement. It has a shallower sensitivity to Earth structure, specifically the elastic parameters V_P , V_S and density ρ (Tanimoto & Rivera 2008; Muir & Tsai 2017), and has been used in joint-inversions with phase velocity dispersion, to constrain both V_P and V_S (Lin *et al.* 2012, 2014). We are therefore interested in its potential for V_P imaging.

Historically, Rayleigh-wave H/V has seen limited use as a seismological imaging tool, perhaps due to the difficulty in obtaining stable measurements (Ferreira & Woodhouse 2007; Tanimoto & Rivera 2008; Ringler *et al.* 2019). However, this has changed in recent years, with many researchers exploring its potential for probing upper-crustal structure, both in the context of classical earthquake seismology (Yano *et al.* 2009; Lin *et al.* 2012; Berbellini *et al.* 2016; Ringler *et al.* 2019) and ambient noise interferometry (Roux 2009; Savage *et al.* 2013; Lin *et al.* 2014; Li *et al.* 2016; Muir & Tsai 2017; Berg *et al.* 2018). In the latter case, horizontal-to-vertical amplitude ratios obtained from multicomponent cross-correlations are interpreted as the Rayleigh-wave H/V ratio, because the correlation signals are believed to contain Rayleigh waves (identified by their elliptical polarization) travelling between pairs of stations. By way of disambiguation, we note that such measurements differ from the 'H/V spectral ratio' obtained from single-station noise records (Nakamura 1989; Fäh *et al.* 2001) which may or may not be related to the Rayleigh-wave H/V ratio (Bonnefoy-Claudet *et al.* 2006). In this paper, we are concerned only with the Rayleigh-wave H/V ratio.

With the maturing of the field of ambient-noise seismology, it is important to rigorously analyse the estimation of Rayleigh H/V ratios from seismic-noise data. The theoretical conditions for Green's-function retrieval from noise correlations are often not satisfied in reality due to non-stationary and heterogeneously distributed noise sources (Stehly *et al.* 2006; Arduin *et al.* 2011, 2015; Erment *et al.* 2017). Consequently, a significant number of studies have warned of inaccurate empirical Green's functions that suffer from artefacts, as well as traveltime and amplitude errors (Halliday & Curtis 2008; Tsai 2009; Yao & van der Hilst 2009; Froment *et al.* 2010; Kimman & Trampert 2010; Tsai 2011; Fichtner 2014). It is therefore to be expected that Rayleigh-wave H/V ratios, which depend on relative amplitudes between components, are also similarly affected. Xu & Mikesell (2017) explicitly confirmed biases in the noise-correlation-derived Rayleigh-wave Green's tensor, which arise from heterogeneous noise sources.

In this study we do not invoke Green's function interpretations for noise-correlation signals; instead we model these signals rigorously for arbitrary spatial distributions of noise sources (Section 2). To our knowledge, no previous study that models cross-correlations in this manner has analysed the Rayleigh H/V measurement in detail. Through a series of synthetic tests, we quantify the dependence of this measurement on the anisotropy of noise-source distribution, as

well as on model V_P , to assess its utility in practice (Sections 3 and 4). Measurement uncertainties, estimated by adding Gaussian noise to synthetic cross-correlation waveforms, shed light on the resolving power with respect to V_P .

2 METHODOLOGY

2.1 Modelling theory

In this section, we describe how the multicomponent CCs are synthesized and used to obtain measurements of H/V ratio. In the frequency domain, ensemble-averaged CCs under the assumption of spatially uncorrelated noise sources (Tromp *et al.* 2010; Sager *et al.* 2018; Fichtner & Tsai 2019) take the general form:

$$C_{pq}(\mathbf{x}_\alpha, \mathbf{x}_\beta) = \int_{\oplus} d\xi G_{pi}^*(\mathbf{x}_\alpha, \xi) G_{qj}(\mathbf{x}_\beta, \xi) S_{ij}(\xi), \quad (1)$$

where $\mathbf{x}_\alpha, \mathbf{x}_\beta$ are the receiver locations; G_{mn} are elements of the Green's tensor satisfying $\mathcal{L}G_{mn}(\mathbf{x}, \xi) = \delta_{mn}\delta(\mathbf{x} - \xi)$ for a wave operator \mathcal{L} (subscripts m and n correspond to the component of motion at the receiver location \mathbf{x} , and the direction of the point force at the source location ξ , respectively); S_{ij} is the power spectral density (PSD) matrix of the noise sources, and the integral is over the Earth volume \oplus . In this study we simplify eq. (1) with a few assumptions. First, noise sources are assumed to be present only on the Earth's surface (e.g. Tromp *et al.* 2010), so the volume integral reduces to a surface integral over its upper boundary Ω , and we can restrict our modelling to just the surface wave part of Green's function. Next, we consider noise sources acting in a single direction only, so the source PSD matrix reduces to a scalar term S . We further assume that the frequency characteristics of S are spatially invariant (Hanasoge 2013, 2014; Datta *et al.* 2019), so that the spatial and frequency dependence of S may be separated, i.e. $S(\xi, \omega) = P(\omega)\sigma(\xi)$. These three simplifications lead to the expression:

$$C_{pq}(\mathbf{x}_\alpha, \mathbf{x}_\beta; \omega) = P(\omega) \int_{\Omega} d\xi G_{pi}^*(\mathbf{x}_\alpha, \xi, \omega) \times G_{qi}(\mathbf{x}_\beta, \xi, \omega) \sigma(\xi). \quad (2)$$

The evaluation of eq. (2) is still a three-step process in general, based on the invocation of source–receiver reciprocity at one of the receiver locations (Tromp *et al.* 2010; Sager *et al.* 2018). However in the specific case of working with a single receiver pair, as in this synthetic study, it is most efficient to invoke reciprocity at both receiver locations (Hanasoge 2014; Xu *et al.* 2019), thereby rewriting eq. (2) as

$$C_{pq}(\mathbf{x}_\alpha, \mathbf{x}_\beta, \omega) = \int_{\Omega} d\xi G_{ip}^*(\xi, \mathbf{x}_\alpha, \omega) \times G_{iq}(\xi, \mathbf{x}_\beta, \omega) P(\omega) \sigma(\xi). \quad (3)$$

Hence C_{pq} is computed as follows. First, we obtain the i -component of impulse response in the entire horizontal domain for sources placed at the receiver locations and acting in the p and q directions. Next, we spatially integrate the product of the two responses (after complex conjugating one of them), weighted by the source mask σ .

This formulation is completely general with regard to the type of Earth model considered and the manner in which the Green's functions are obtained (e.g. analytically or numerically). In our implementation, we work with 1-D, vertically stratified media for which surface wave terms of the elastodynamic Green's tensor are semi-analytically computable in 2-D as well as 3-D.

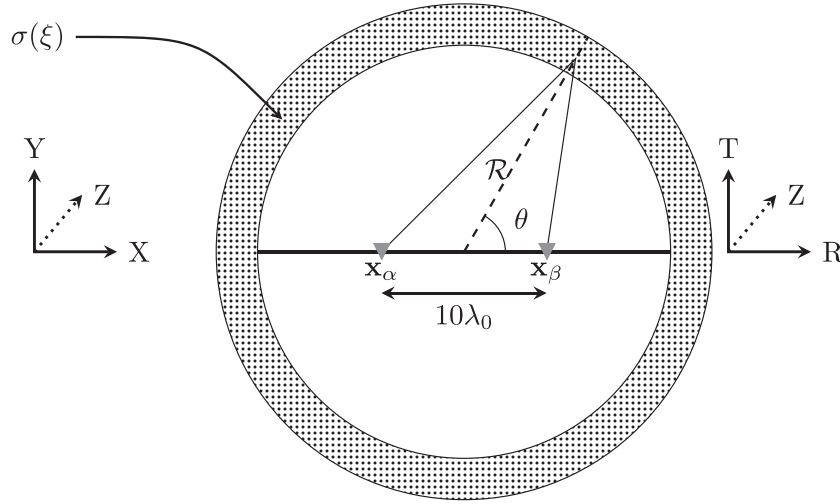


Figure 1. Schematic showing arrangement of sources (dots) and receivers (inverted triangles) in the modelling domain Ω . The coordinate axes R , T and Z represent the radial, transverse and vertical directions, respectively, for the receiver pair.

2.2 Computation of the Green's function

In our forward modelling scheme, we use a source direction i set to either z (vertical direction) or x (radial direction, see Fig. 1), which corresponds to excitation of Rayleigh waves alone, or both Rayleigh and Love waves, respectively. In laterally homogeneous media, the Rayleigh- and Love-wave terms of Green's function for a point source at $x = y = 0, z = h$, are (Aki & Richards 2002, section 7.4):

$$\mathbf{G}^{\text{RAY}}(x, y, z) = \sum_n \frac{1}{8cUI_1} \times \begin{bmatrix} r_1(h)r_1(z)\frac{x^2}{r^2} & r_1(h)r_1(z)\frac{xy}{r^2} & -ir_2(h)r_1(z)\frac{x}{r} \\ r_1(h)r_1(z)\frac{xy}{r^2} & r_1(h)r_1(z)\frac{y^2}{r^2} & -ir_2(h)r_1(z)\frac{y}{r} \\ ir_1(h)r_2(z)\frac{x}{r} & ir_1(h)r_2(z)\frac{y}{r} & r_2(h)r_2(z) \end{bmatrix} \times H_0^{(1)}(k_n r) \quad (4)$$

$$\mathbf{G}^{\text{LOV}}(x, y, z) = \sum_n \frac{l_1(h)l_1(z)}{8cUI_1} \begin{bmatrix} \frac{y^2}{r^2} & \frac{-xy}{r^2} & 0 \\ \frac{-xy}{r^2} & \frac{x^2}{r^2} & 0 \\ 0 & 0 & 0 \end{bmatrix} \times H_0^{(1)}(k_n r). \quad (5)$$

Here, r_1, r_2 (Rayleigh) and l_1 (Love) are displacement eigenfunctions and we write $r = \sqrt{x^2 + y^2}$. All symbols follow the Aki & Richards (2002) convention. However, our expressions are different inasmuch as we use Cartesian rather than cylindrical coordinates (we work with a Cartesian grid ξ), and abandon the far-field approximation. The Hankel function of the first kind, $H_0^{(1)}$, is used instead of its asymptotic form, because the implementation of (3) necessitates computation of Green's function at distances comparable to or shorter than a wavelength (see Section 3.1).

To evaluate expressions (4) and (5), we solve the surface wave eigenvalue problem by the method of Gombert & Masters (1988), as in Datta *et al.* (2017) and Datta (2018). This gives phase velocity c , group velocity U and the eigenfunctions r_1, r_2 and l_1 , which are numerically integrated to obtain the energy integral I_1 . Since we only need to evaluate \mathbf{G} for sources and receivers on the surface, we use $h = z = 0$.

2.3 H/V ratio measurement

Rayleigh waves are polarized in the radial-vertical (R - Z) plane and their H/V ratio refers to the ratio η of the radial to vertical displacement amplitudes (e.g. Maupin 2017). In a laterally homogeneous medium, η is easily obtained from the displacement eigenfunctions evaluated at the surface. By definition,

$$\eta(\omega) = \frac{r_1(z=0, \omega)}{r_2(z=0, \omega)}. \quad (6)$$

Equivalently, one may write

$$\eta = \frac{|G_{RR}|}{|G_{ZZ}|} = \frac{|G_{RR}|}{|G_{ZR}|}. \quad (7)$$

The equivalence between eqs (7) and (6) is seen from eq. (4), when the x, y axes are oriented along the radial and transverse directions respectively (e.g. Fig. 1). Since the second index in the Green's tensor G_{ij} refers to the source orientation, eq. (7) asserts that η is a medium property, independent of whether the source (point-force) is vertical or radial.

In the case of ambient noise CCs, most studies define the Rayleigh H/V ratio analogously to eq. (7) using the corresponding elements of the cross-correlation tensor: $C_{RR}, C_{ZZ}, C_{ZR}, C_{RZ}$. Since CCs are usually obtained after some pre-processing of raw noise records (e.g. Bensen *et al.* 2007), it is important that any normalization is applied uniformly across different components, so as to preserve the relative amplitudes between them (Lin *et al.* 2014; Muir & Tsai 2017). In this study, we work only with synthetics so there is no processing, but we note that all analogies with real-data scenarios require that multicomponent seismic records be processed collectively rather than independently.

If equivalence between cross-correlations and Green's function holds, the two CC measurements, Γ^R and Γ^Z , correspond to virtual sources oriented radially and vertically respectively, as indicated by their superscripts:

$$\begin{aligned} \Gamma^R &= \frac{f(C_{RR})}{f(C_{ZR})} \sim \eta \\ \Gamma^Z &= \frac{f(C_{RZ})}{f(C_{ZZ})} \sim \eta. \end{aligned} \quad (8)$$

Here, the function f on the right-hand side represents operations applied on the CCs to obtain robust measurements. In this study, we

(1) determine the envelope of the cross-correlation signal, (2) pick its maximum value on the causal and anticausal branches and (3) average the two values thus obtained.

On the other hand, since cross-correlations and Green's functions are not necessarily equivalent (e.g. when source illumination is anisotropic), we define a third measurement Γ , which does not afford an interpretation in terms of a virtual source. It is the ratio between C_{RR} and C_{ZZ} . From the forward model (2), we have:

$$\begin{aligned} C_{RR} &\propto \int G_{RZ}^* G_{RZ} \\ C_{ZZ} &\propto \int G_{ZZ}^* G_{ZZ} \end{aligned} \quad (9)$$

when $i = Z$ in (2), or

$$\begin{aligned} C_{RR} &\propto \int G_{RR}^* G_{RR} \\ C_{ZZ} &\propto \int G_{ZR}^* G_{ZR} \end{aligned} \quad (10)$$

when $i = R$. Therefore it is expected that C_{RR}/C_{ZZ} is proportional to G_{RZ}^2/G_{ZZ}^2 when noise sources are vertical, and to G_{RR}^2/G_{ZR}^2 when sources act along the radial direction for a given receiver pair. In general, given the definition (7), we estimate that Γ is related to the square of the classical Rayleigh-wave H/V:

$$\Gamma = \frac{f(C_{RR})}{f(C_{ZZ})} \sim \eta^2. \quad (11)$$

3 SIMULATIONS

We perform a suite of simulations designed to empirically assess the sensitivity of H/V measurements to V_p structure, as well as gross geometrical features of the noise-source distribution σ . These are the two quantities which we vary in our forward modelling, while other parameters are held fixed. As explained in the previous section, our modelling scheme entails a 1-D, depth-dependent Earth model $M(z)$ in which the Green's functions are computed, and a 2-D horizontal domain $\Omega(x, y)$ on which the sources are distributed (the Earth model is implicitly uniform throughout Ω). Here we first describe the fixed parameters, pertaining to Ω , and then the model variations, which involve both M and Ω .

3.1 Fixed parameters

Rayleigh-wave H/V ratio is a frequency-dependent quantity but for the sake of simplicity, (most) results presented in this paper correspond to a single frequency, $f_0 = 0.1$ Hz. This value (10 s period) is chosen because it lies in between the primary and secondary microseism peaks at ~ 7 and 15 s (Peterson 1993; Arduin *et al.* 2015). This choice of frequency dictates nearly all other choices relating to the simulation geometry. We model the PSD of the noise sources, $P(\omega)$, with a narrow-band Gaussian centred at $f_0 = 0.1$ Hz (see Fig. 3f). The corresponding wavelength, λ_0 , is used to fix the uniform grid spacing $\Delta h \leq \lambda_0/4$ and separation between receivers, $|\mathbf{x}_\alpha - \mathbf{x}_\beta| \geq 10\lambda_0$, well above the typical requirement of three wavelengths (Bensen *et al.* 2007; Luo *et al.* 2015). The size of the domain Ω is chosen to be at least twice the receiver separation in both directions, i.e., $[x_{\min}, x_{\max}, y_{\min}, y_{\max}] = 20\lambda_0 \times [-1, 1, -1, 1]$.

We have $\lambda_0 \approx 32.8$ km for Earth model M_0 (see section 3.2), which leads to the values $\Delta h = 5$ km, $\mathbf{x}_\alpha = (-162.5 \text{ km}, 0)$, $\mathbf{x}_\beta = (162.5 \text{ km}, 0)$ and $\Omega = \{-600 \text{ km} < x < 600 \text{ km}, -600 \text{ km} < y < 600 \text{ km}\}$. Note that the receivers are kept off-grid, since our

implementation (3) places sources at their locations, and Green's functions (4), (5) blow up at the source. Finally, we use a temporal sampling interval of 1 s and generate a time-series of length 400 s.

3.2 Models used

The 1-D Earth model used for the simulations is derived from the global CRUST2.0 model (Bassin 2000), by extracting it at the location (60°N, 60°E) where the crust is relatively thick at 50 km. We call this model M_0 . Simulations are performed for 21 variants of this model, which differ only in their V_p values—a relative perturbation in the range -10 to $+10$ per cent is applied uniformly at all depths to the model V_p .

Each Earth model M is used in conjunction with a particular model for the source distribution σ over the domain Ω . We use different classes of σ . *Uniform distribution* where the sources have uniform strength everywhere in the domain; *Ring distribution* where sources are present at some distance (\mathcal{R}) from the centre of domain within a strip of width $d\mathcal{R}$ Fig. 1, and *Arc distribution* where sources are confined to an arc, with given \mathcal{R} and $d\mathcal{R}$, oriented at some angle to the receiver pair. We use $\mathcal{R} = 500$ km and $d\mathcal{R} = 40$ km for ring and arc distributions. Three arc distributions are implemented to cover the range of possible scenarios of source directionality with respect to the receiver pair: *parallel* ($\theta = -15^\circ$ to 15°), *oblique* ($\theta = 30^\circ$ to 60°) and *orthogonal* ($\theta = 75^\circ$ to 105°). The arcs have uniform source strength in the aforementioned ranges for θ , but are cosine tapered to zero over an additional 5° at both ends.

The five source-distribution models utilized for the simulations are shown in Fig. 2.

4 ANALYSIS AND RESULTS

We start by examining the CC obtained for each of the noise-source distributions in Earth model M_0 . These are shown in Fig. 3 for vertically oriented sources and fundamental-mode Rayleigh waves ($n = 0$ in eq. (4)). The effect of anisotropic source distributions is readily observed on the amplitude (in positive and negative branches, A^+ , A^-) as well as arrival time (T_{CC}) of signals in the CC. Uniform and ring distributions show $A^+ = A^-$ and nearly the same arrival times as for Rayleigh waves (T_R) with one of the receivers acting as a virtual source. In contrast, the arc-type distributions have $A^+ \neq A^-$ and $T_{CC} = T_R$ holds only for the parallel-arc configuration. These observations are well understood in terms of stationary and non-stationary phase sources (e.g. Xu & Mikesell 2017). Supporting Information Fig. S1 shows the corresponding results for horizontal sources.

Next, we look at various H/V measurements obtained for all our Earth models with varying V_p . Simulations are performed separately for vertical and horizontal sources. The former act in the z -direction and excite Rayleigh waves only, hence are denoted 'zR'; the latter act in the x -direction and excite both Love and Rayleigh waves, hence are denoted 'xRL'. Fig. 4 shows H/V as a function of V_p , for different noise source distributions, and for zR as well as xRL simulations. We find that for zR, H/V measurements for the uniform and ring distributions have an excellent match with the theoretical Rayleigh-wave H/V ratio, that is $\Gamma^R = \Gamma^Z \approx \eta$ and $\Gamma \approx \eta^2$. On the question of sensitivity to V_p , this implies that Γ offers better resolution than Γ^R or Γ^Z — the 'dynamic range' of η , i.e. the difference between its maximum and minimum values over the range of Earth models used, is $\eta_{DR} \approx 0.085$ whereas for η^2 it is slightly higher, $\eta^2_{DR} \approx 0.104$ (also apparent from the slopes of the graphs). For xRL, there

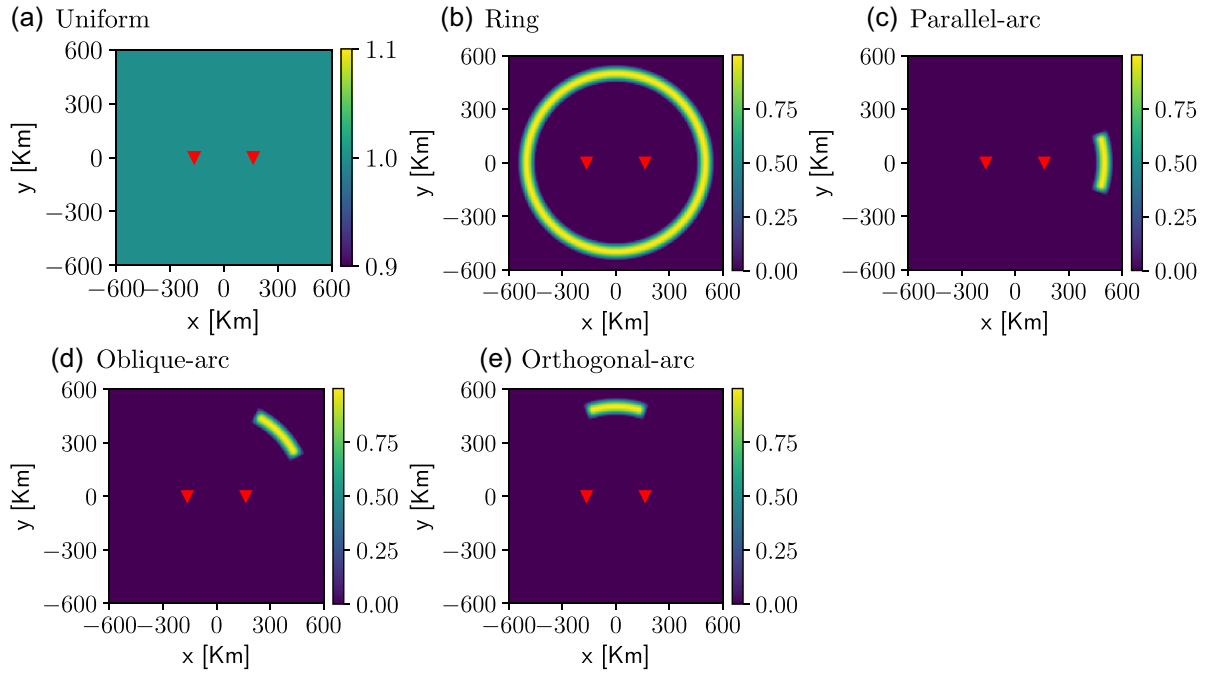


Figure 2. Different noise source distributions as defined in the text and identified here by the individual plot titles. The red triangles mark the receiver locations.

is a systematic offset between the Γ -curves and the η -curves in case of the uniform distribution, while the ring distribution case shows reasonable agreement.

Moving on to the anisotropic (arc-type) noise source distributions, there is reasonable agreement with theory only in the zR, parallel-arc case. All other cases exhibit a breakdown of the equivalence relations between the CC-derived H/V and the theoretical Rayleigh-wave H/V. For xRL, the highly deviant measurements in the oblique- and orthogonal-arc scenarios are expected, due to strong Love-wave components along the radial direction between the receivers. In the parallel-arc case, the discrepancies are much lower but still significant, because they are comparable to the dynamic range of the theoretical H/V. This observation is noteworthy because many studies deal with the issue of anisotropic noise sources, by only incorporating receiver pairs that are aligned with the dominant source illumination direction, which is often constrained only in a qualitative sense. Fig. 4(f) suggests that very tight constraints on noise sources-receiver pair alignment are required to avoid Love-wave contamination in CC-derived H/V measurements. We note that the condition $\Gamma^R = \Gamma^Z$ holds for all source distributions except the orthogonal-arc in the zR case, and for all distributions except the oblique- and orthogonal-arcs in the xRL case.

We also analysed the sensitivity of H/V to perturbations at different depths, by perturbing each layer in the model separately, rather than whole-model perturbations as described above. These tests, shown in Supporting Information Figs S3–S5, confirm the well-known shallow sensitivity of Rayleigh-wave H/V. Model perturbations in the first layer, down to 17 km depth, dominate the impact on H/V, with deeper perturbations having little impact except at longer periods.

Finally, inclusion of higher modes in our analyses did not provide additional insight, due to the order-of-magnitude weaker excitation of higher modes for the types of sources and model considered.

4.1 Measurements with added synthetic noise

The excitation of ambient noise in the Earth is a stochastic process and, when working with real data, seismologists typically use an ‘ensemble average’ over a large number of cross-correlations (by stacking CC waveforms over various durations of time, from days or weeks to several months) as the basic measurement from which useful inferences can be derived. Therefore in practice, there is always a ‘realization noise’ associated with ambient noise CC-derived measurements. This constitutes a random noise level in ambient noise data, which is always present. Thus, no matter how accurate the source or structure models are, predicted and observed cross-correlations will always be different because of realization noise. In this study, one of our aims is to assess the sensitivity of H/V measurements to V_P , and so we compare it to estimates of noise levels in the data.

To this end, we compute synthetic estimates of measurement uncertainty in the present section by adding random noise to our synthetic CC waveforms. The magnitudes of uncertainties, compared with the dynamic range of the measurements (over the range of V_P values considered) sheds light on the usefulness of these measurements in practice. We note that numerical simulations with added random noise have been used in the literature to simulate ensemble cross-correlations (Cupillard & Capdeville 2010).

We obtain noisy synthetic waveforms $\tilde{s}(t)$, by adding noise $N(t)$, of chosen strength, to the noise-free signal $s(t)$, as

$$\tilde{s}(t) = s(t) + \frac{\alpha k}{100} N(t), \quad (12)$$

where α is the desired signal-to-noise ratio and k is a scaling factor to bring the noise amplitudes to the signal level. N is computed in the frequency domain, using the power spectrum of the signal:

$$N(\omega) = P(\omega)\chi(\omega), \quad (13)$$

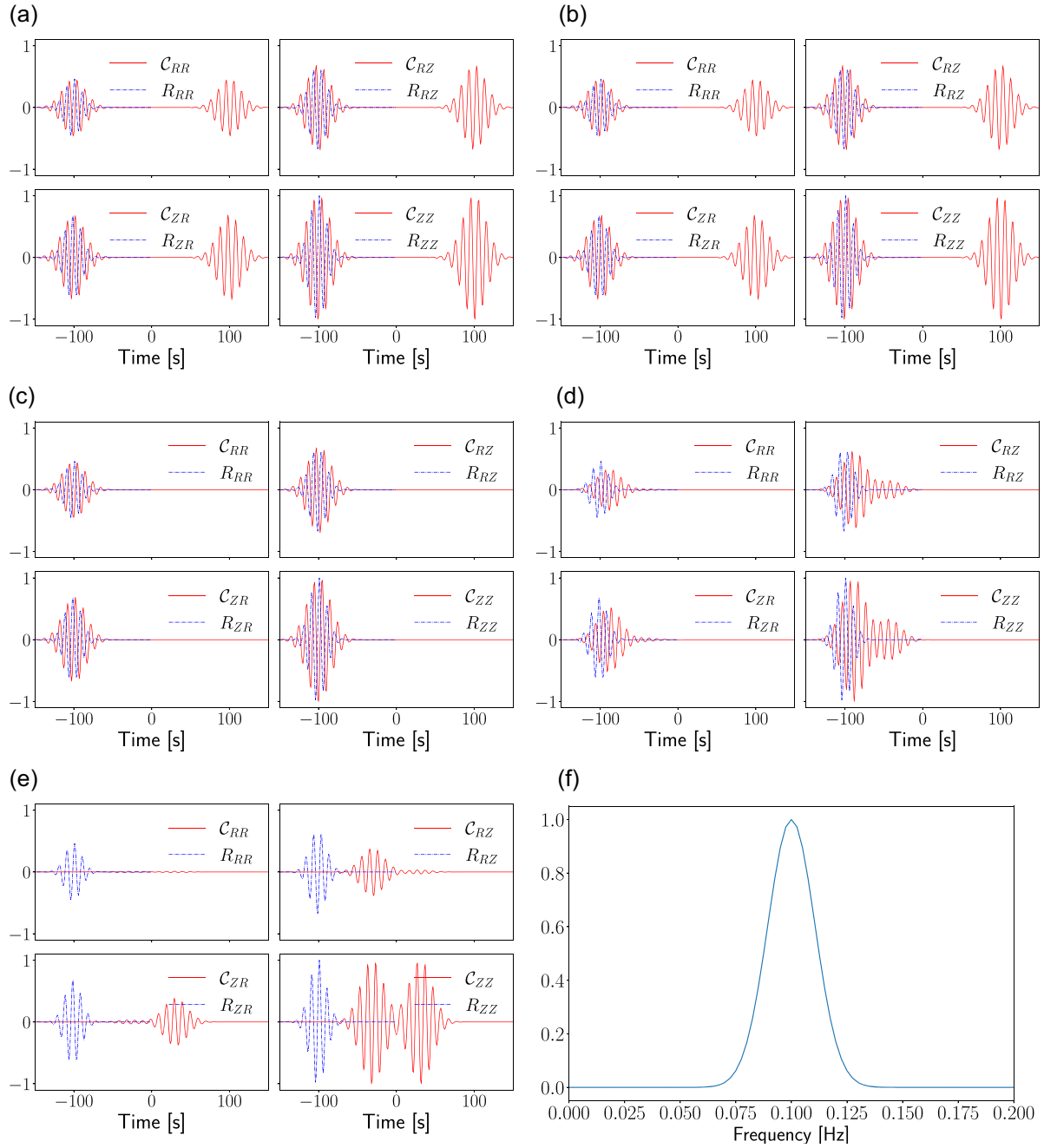


Figure 3. Panels (a)–(e) show the synthetic CCs generated for the corresponding source distributions in Fig. 2, with ‘zR’ source excitation. Each panel contains four plots for the four components (clockwise from top left) C_{RR} , C_{RZ} , C_{ZZ} and C_{ZR} . The corresponding Rayleigh wave from x_α to x_β has also been presented for comparison. The amplitudes are normalized with respect to the maximum within a panel. (f) $P(\omega)$ for the noise sources, centred at 0.1 Hz.

where $P(\omega) = s^*(\omega)s(\omega)$, $\chi(\omega) = [\mathcal{N}(0, 1) + j\mathcal{N}(0, 1)]/\sqrt{2}$ and $\mathcal{N}(\mu, \sigma)$ represents a Gaussian random variable with mean, μ , and standard deviation, σ (not to be confused with the source mask defined earlier).

H/V ratio calculations are performed for a given amount of noise (viz. 2, 5 and 10 per cent) and for each source distribution and Earth model, using all three H/V ratios, that is eqs (8) and (11). The results are shown in Fig. 5 (for the zR case; xRL case shown in Supporting Information Fig. S2), with standard error estimated from 1000 realizations of added random noise.

As in the noise-free case, the mean trend of estimated H/V ratio in the presence of added noise closely follows the theoretical curves for homogeneous, ring and parallel-arc distributions. For the oblique-arc distribution there is a significant departure of mean trend from the theoretical curves containing a large error. For the orthogonal-arc distribution the H/V observation are completely erroneous. The uncertainty in estimated H/V ratios (Γ^R , Γ^Z , and Γ) in the presence of noise helps us evaluate the efficacy of measurements based on the thresholds given by η_{DR} for Γ^R and Γ^Z , and by η^2_{DR} for Γ . We infer two things from the observed values. First, meaningful measurements can only be made for up to 10 per cent random

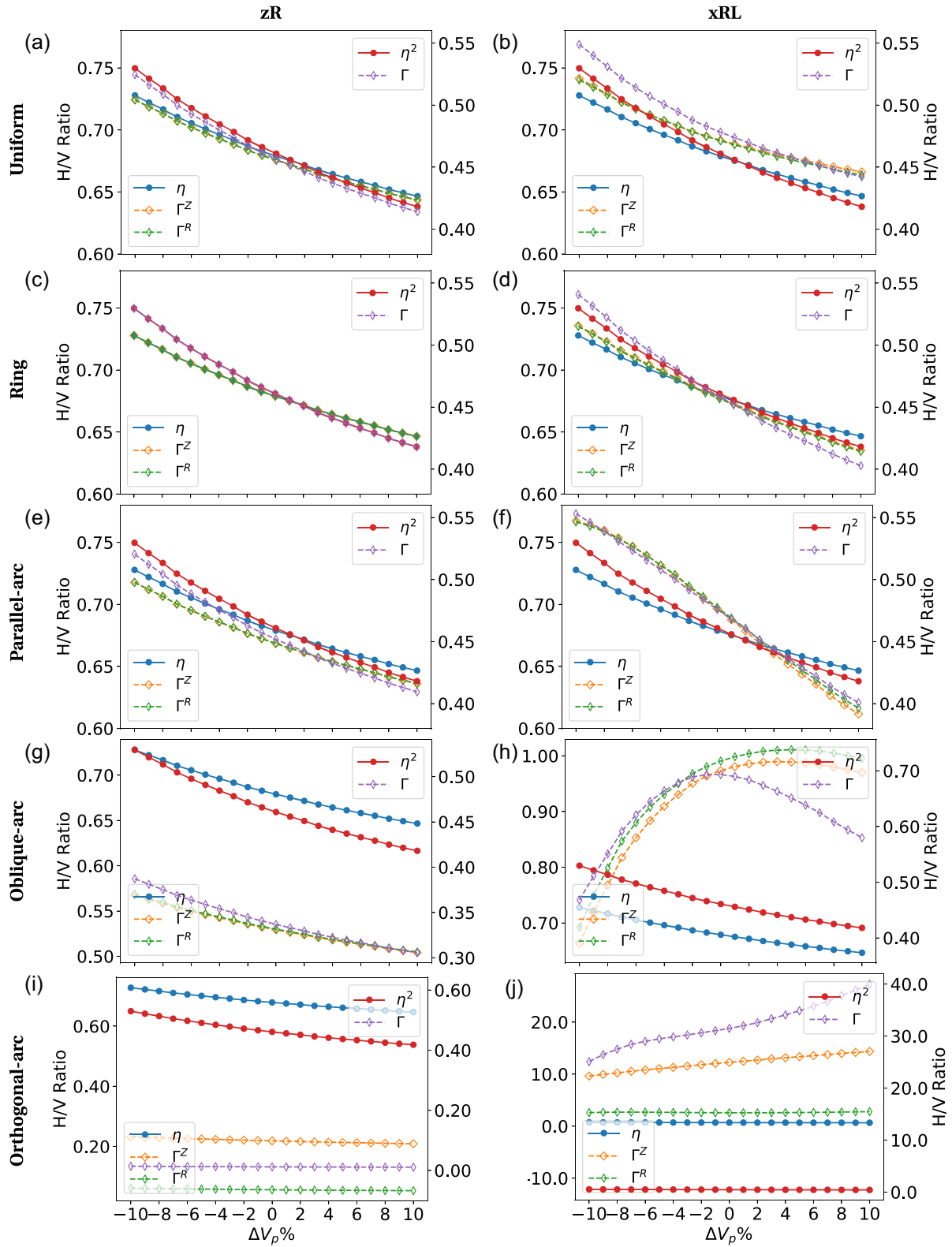


Figure 4. H/V ratio as a function of model V_p , for different noise source distributions along rows (labels on the left-hand side) and the two different source excitations along columns (labels at the top). In each plot, the CC-derived measurements (lines with diamonds) are compared with the theoretical Rayleigh-wave H/V for the medium (lines with circles), the latter being the same in all plots. Note that we have used separate y-axes for different curves, shown on the left and right-hand sides of each plot. The legend boxes attached to these two axes identify the curves associated.

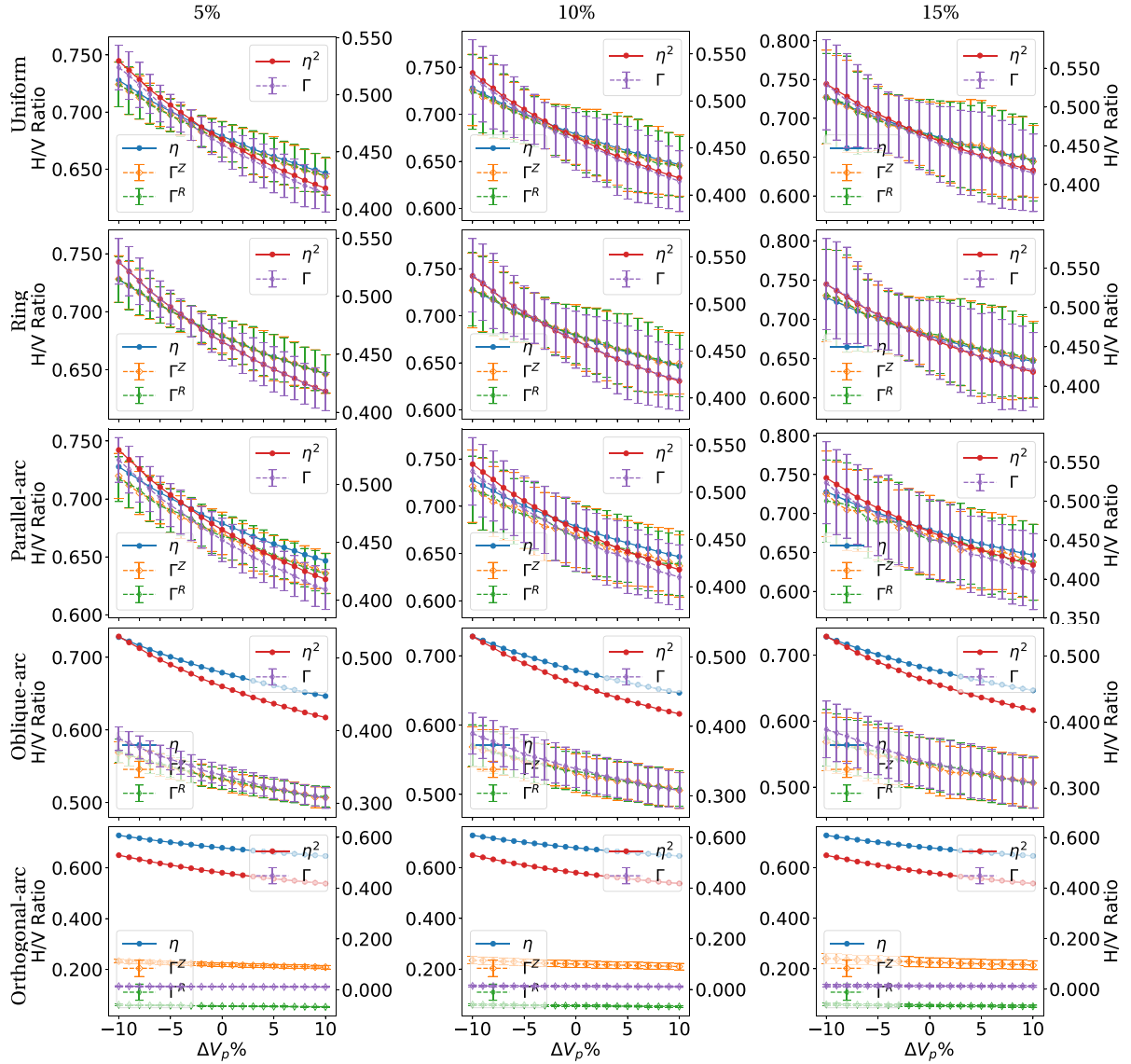


Figure 5. Similar to Fig. 4 but for measurements made with synthetic noise added to the CC, for zR source excitation. Noise levels vary across columns as indicated in the top panel, and rows correspond to source distributions as indicated on the extreme left.

Gaussian noise. Beyond this noise level, the uncertainties in CC-derived H/V ratios reach or exceed the η_{DR} or η^2_{DR} thresholds. Second, noise has a lower impact on Γ in comparison to Γ^R and Γ^Z , due to its larger dynamic range.

5 DISCUSSION AND CONCLUSIONS

We have presented a synthetic study that critically examines measurements commonly used to estimate the Rayleigh-wave ellipticity or H/V ratio, from multicomponent CCs of ambient noise recordings. In practice these measurements may be expected to be influenced by a variety of factors—anisotropic noise source illumination, interference from Love waves or higher-mode surface waves, and complicated wave propagation effects due to heterogeneous Earth structure. Our numerical study investigates some of these factors whilst simultaneously assessing the sensitivity of these measurements to V_p structure. It is based on (quasi) full-wave modelling of noise CCs in a 1-D elastic medium, and leads to the following conclusions:

(i) Relative amplitudes between different components of the CC tensor, particularly those used to compute H/V, are biased by anisotropically distributed noise sources. Unless the pre-processing techniques are capable of satisfactorily mitigating the spatial variability of noise sources, this bias cannot be eliminated (note that we apply no additional processing in this synthetic study).

(ii) Love-wave contributions, if present in the ambient noise field, produce a significant bias which is negligible only for highly favourable, and therefore likely unrealistic, distributions of noise sources.

(iii) H/V measurements do show sensitivity to V_p , but these may be easily undermined by data uncertainties on the order ~ 10 per cent or higher.

(iv) Sensitivity to V_p may be enhanced by using the measurement $\Gamma = C_{RR}/C_{ZZ}$, which recovers the square of the Rayleigh-wave H/V ratio when noise sources are favourably distributed.

To deepen the understanding gained in this study, as well as to overcome the limitations of the EGF approach highlighted herein,

we advocate constructing (finite-frequency) sensitivity kernels for Γ^R , Γ^Z , Γ , using the forward model eq. (2). In particular, this will provide insight into the hitherto unexplored Γ measurement, which defies conventional interpretation in an EGF framework. In general, this will allow for all types of measurements to be used in practice without the biases inherent in the EGF approach.

The need for treating these measurements as independent observables, outside the EGF framework, is only amplified by consideration of 3-D structural effects, which we did not model in this study. We have shown the contamination of noise CC-derived H/V measurements due to features of the ambient noise source field alone. Additional contamination is expected from lateral variations in Earth structure, which can cause scattering and path bending, potentially tilting the particle polarization away from the R – Z plane. All of these complexities argue in favour of modelling cross-correlation rigorously (as in eq. 2) and using the same forward model to derive sensitivity kernels for any measurement of interest. These kernels will honour the measurement for what it is, minimizing the danger of misinterpretation and leading to a better-posed, if more involved, inverse problem. Construction of such finite-frequency sensitivity kernels is the subject of ongoing research.

ACKNOWLEDGEMENTS

This work was funded by Shell India Markets Pvt. Ltd. AD acknowledges support from Shell contract PT75508 while at TIFR. We are grateful to the two anonymous reviewers whose comments helped to substantially improve this manuscript.

DATA AVAILABILITY

No new data were generated or analysed in support of this research.

REFERENCES

- Aki, K. & Richards, P.G., 2002. *Quantitative Seismology*, University Science Books.
- Arduin, F., Stutzmann, E., Schimmel, M. & Mangeney, A., 2011. Ocean wave sources of seismic noise, *J. geophys. Res.*, **116**(C9), C09004, doi:10.1029/2011JC006952.
- Arduin, F., Gualtieri, L. & Stutzmann, E., 2015. How ocean waves rock the Earth: two mechanisms explain microseisms with periods 3 to 300 s, *Geophys. Res. Lett.*, **42**(3), 765–772.
- Bassin, C., 2000. The current limits of resolution for surface wave tomography in North America, *EOS, Trans. Am. geophys. Un.*, **81**, F897.
- Bensen, G.D., Ritzwoller, M.H., Barmin, M.P., Levshin, A.L., Lin, F., Moschetti, M.P., Shapiro, N.M. & Yang, Y., 2007. Processing seismic ambient noise data to obtain reliable broad-band surface wave dispersion measurements, *Geophys. J. Int.*, **169**(3), 1239–1260.
- Berbellini, A., Morelli, A. & Ferreira, A. M.G., 2016. Ellipticity of Rayleigh waves in basin and hard-rock sites in Northern Italy, *Geophys. J. Int.*, **206**(1), 395–407.
- Berg, E., Lin, F.-C., Allam, A., Qiu, H., Shen, W. & Ben-Zion, Y., 2018. Tomography of Southern California via Bayesian joint inversion of Rayleigh wave ellipticity and phase velocity from ambient noise cross-correlations, *J. geophys. Res.*, **123**(11), 9933–9949.
- Bonnefoy-Claudet, S., Cornou, C., Bard, P.Y., Cotton, F., Moczo, P., Kristek, J. & Fäh, D., 2006. H/V ratio: a tool for site effects evaluation. Results from 1-D noise simulations, *Geophys. J. Int.*, **167**(2), 827–837.
- Cupillard, P. & Capdeville, Y., 2010. On the amplitude of surface waves obtained by noise correlation and the capability to recover the attenuation: a numerical approach, *Geophys. J. Int.*, **181**(3), 1687–1700.
- Datta, A., 2018. SWRT: a package for semi-analytical solutions of surface wave propagation, including mode conversion, across transversely aligned vertical discontinuities, *Geosci. Instrum. Methods Data Syst.*, **7**(1), 101–112.
- Datta, A., Priestley, K.F., Roecker, S. & Chapman, C.H., 2017. Surface wave mode coupling and the validity of the path average approximations in surface waveform inversions: an empirical assessment, *Geophys. J. Int.*, **211**(2), 1099–1120.
- Datta, A., Hanasoge, S. & Goudswaard, J., 2019. Finite frequency inversion of cross-correlation amplitudes for ambient noise source directivity estimation, *J. geophys. Res.*, **124**, 6653–6665.
- Ermert, L., Sager, K., Afanasiev, M., Boehm, C. & Fichtner, A., 2017. Ambient seismic source inversion in a heterogeneous Earth: theory and application to the Earth's hum, *J. geophys. Res.*, **122**(11), 9184–9207.
- Fäh, D., Kind, F. & Giardini, D., 2001. A theoretical investigation of average H/V ratios, *Geophys. J. Int.*, **145**(2), 535–549.
- Ferreira, A.M.G. & Woodhouse, J.H., 2007. Observations of long period Rayleigh wave ellipticity, *Geophys. J. Int.*, **169**(1), 161–169.
- Fichtner, A., 2014. Source and processing effects on noise correlations, *Geophys. J. Int.*, **197**(3), 1527–1531.
- Fichtner, A. & Tsai, V.C., 2019. Theoretical foundations of noise interferometry, in *Seismic Ambient Noise*, 1st edn, pp. 109–143, eds Nakata, N., Gualtieri, L. & Fichtner, A., Cambridge Univ. Press.
- Froment, B., Campillo, M., Roux, P., Gouédard, P., Verdel, A. & Weaver, R.L., 2010. Estimation of the effect of nonisotropically distributed energy on the apparent arrival time in correlations, *Geophysics*, **75**(5), SA85–SA93.
- Gomberg, J.S. & Masters, T.G., 1988. Waveform modelling using locked-mode synthetic and differential seismograms: application to determination of the structure of Mexico, *Geophys. J. Int.*, **94**(2), 193–218.
- Halliday, D. & Curtis, A., 2008. Seismic interferometry, surface waves and source distribution, *Geophys. J. Int.*, **175**(3), 1067–1087.
- Hanasoge, S.M., 2013. The influence of noise sources on cross-correlation amplitudes, *Geophys. J. Int.*, **192**(1), 295–309.
- Hanasoge, S.M., 2014. Measurements and kernels for source-structure inversions in noise tomography, *Geophys. J. Int.*, **196**, 971–985.
- Kimman, W.P. & Trampert, J., 2010. Approximations in seismic interferometry and their effects on surface waves, *Geophys. J. Int.*, **182**(1), 461–476.
- Li, G., Chen, H., Niu, F., Guo, Z., Yang, Y. & Xie, J., 2016. Measurement of Rayleigh wave ellipticity and its application to the joint inversion of high-resolution s wave velocity structure beneath northeast China, *J. geophys. Res.*, **121**(2), 864–880.
- Lin, F.-C., Schmandt, B. & Tsai, V.C., 2012. Joint inversion of Rayleigh wave phase velocity and ellipticity using USArray: constraining velocity and density structure in the upper crust, *Geophys. Res. Lett.*, **39**(12), L12303, doi:10.1029/2012GL052196.
- Lin, F.C., Tsai, V.C. & Schmandt, B., 2014. 3-D crustal structure of the western United States: application of Rayleigh-wave ellipticity extracted from noise cross-correlations, *Geophys. J. Int.*, **198**(2), 656–670.
- Liu, Q. *et al.*, 2016. Source locations of teleseismic P, SV, and SH waves observed in microseisms recorded by a large aperture seismic array in China, *Earth planet. Sci. Lett.*, **441**, 39–47.
- Luo, Y., Yang, Y., Xu, Y., Xu, H., Zhao, K. & Wang, K., 2015. On the limitations of interstation distances in ambient noise tomography, *Geophys. J. Int.*, **201**(2), 652–661.
- Maupin, V., 2017. 3-D sensitivity kernels of the Rayleigh wave ellipticity, *Geophys. J. Int.*, **211**(1), 107–119.
- Muir, J.B. & Tsai, V.C., 2017. Rayleigh-wave H/V via noise cross correlation in Southern California, *Bull. seism. Soc. Am.*, **107**(5), 2021–2027.
- Nakamura, Y., 1989. A method for dynamic characteristics estimation of subsurface using microtremor on the ground surface, *Q. Rep. Railw. Tech. Res. Inst.*, **30**(1), 25–33.
- Nakata, N., Chang, J.P., Lawrence, J.F. & Boué, P., 2015. Body wave extraction and tomography at Long Beach, California, with ambient-noise interferometry, *J. geophys. Res.*, **120**(2), 1159–1173.
- Nakata, N., Boué, P., Brenguier, F., Roux, P., Ferrazzini, V. & Campillo, M., 2016. Body and surface wave reconstruction from seismic noise correlations between arrays at Piton de la Fournaise volcano, *Geophys. Res. Lett.*, **43**(3), 1047–1054.

- Pedersen, H.A. & Colombi, A., 2018. Body waves from a single source area observed in noise correlations at arrival times of reflections from the 410 discontinuity, *Geophys. J. Int.*, **214**, 1125–1135.
- Peterson, J.R., 1993. Observations and modeling of seismic background noise, Open-File Rep, U.S. Geol. Surv., 93-322.
- Poli, P., Pedersen, H.A. & Campillo, M., 2012. Emergence of body waves from cross-correlation of short period seismic noise, *Geophys. J. Int.*, **188**(2), 549–558.
- Ringler, A.T., Wilson, D.C., Zürn, W. & Anthony, R.E., 2019. Rayleigh wave ellipticity measurement uncertainty across the IRIS/USGS and New China Digital Seismograph Networks, *Geophys. J. Int.*, **217**(1), 219–237.
- Roux, P., 2009. Passive seismic imaging with directive ambient noise: application to surface waves and the San Andreas Fault in Parkfield, CA, *Geophys. J. Int.*, **179**(1), 367–373.
- Roux, P., Sabra, K.G., Gerstoft, P., Kuperman, W.A. & Fehler, M.C., 2005. P-waves from cross-correlation of seismic noise, *Geophys. Res. Lett.*, **32**(19), L19303, doi:10.1029/2005GL023803.
- Sager, K., Ermert, L., Boehm, C. & Fichtner, A., 2018. Towards full wave-form ambient noise inversion, *Geophys. J. Int.*, **212**(1), 566–590.
- Savage, M.K., Lin, F.-C. & Townend, J., 2013. Ambient noise cross-correlation observations of fundamental and higher-mode Rayleigh wave propagation governed by basement resonance, *Geophys. Res. Lett.*, **40**(14), 3556–3561.
- Saygin, E., Cummins, P.R. & Lumley, D., 2017. Retrieval of the P wave reflectivity response from autocorrelation of seismic noise: Jakarta Basin, Indonesia, *Geophys. Res. Lett.*, **44**(2), 792–799.
- Shapiro, N.M. & Campillo, M., 2004. Emergence of broadband Rayleigh waves from correlations of the ambient seismic noise, *Geophys. Res. Lett.*, **31**(7), doi:10.1029/2004GL019491.
- Snieder, R., 2004. Extracting the Green's function from the correlation of coda waves: a derivation based on stationary phase, *Phys. Rev. E*, **69**(4), 046610.
- Stehly, L., Campillo, M. & Shapiro, N.M., 2006. A study of the seismic noise from its long-range correlation properties, *J. geophys. Res.*, **111**(B10), B10306.
- Tanimoto, T. & Rivera, L., 2008. The ZH ratio method for long-period seismic data: sensitivity kernels and observational techniques, *Geophys. J. Int.*, **172**(1), 187–198.
- Tromp, J., Luo, Y., Hanasoge, S. & Peter, D., 2010. Noise cross-correlation sensitivity kernels, *Geophys. J. Int.*, **183**(2), 791–819.
- Tsai, V.C., 2009. On establishing the accuracy of noise tomography travel-time measurements in a realistic medium, *Geophys. J. Int.*, **178**(3), 1555–1564.
- Tsai, V.C., 2011. Understanding the amplitudes of noise correlation measurements, *J. geophys. Res.*, **116**(B9), B09311, doi:10.1029/2011JB008483.
- Wang, W., Gerstoft, P. & Wang, B., 2018. Seasonality of P wave microseisms from NCF-based beamforming using ChinArray, *Geophys. J. Int.*, **213**(3), 1832–1848.
- Weaver, R.L. & Lobkis, O.I., 2004. Diffuse fields in open systems and the emergence of the Green's function (L), *J. acoust. Soc. Am.*, **116**(5), 2731–2734.
- Xu, Z. & Mikesell, T.D., 2017. On the reliability of direct Rayleigh-wave estimation from multicomponent cross-correlations, *Geophys. J. Int.*, **210**(3), 1388–1393.
- Xu, Z., Mikesell, T.D., Gribler, G. & Mordret, A., 2019. Rayleigh-wave multicomponent cross-correlation-based source strength distribution inversion. Part 1: theory and numerical examples, *Geophys. J. Int.*, **218**(3), 1761–1780.
- Yano, T., Tanimoto, T. & Rivera, L., 2009. The ZH ratio method for long-period seismic data: inversion for S-wave velocity structure, *Geophys. J. Int.*, **179**(1), 413–424.
- Yao, H. & van der Hilst, R.D., 2009. Analysis of ambient noise energy distribution and phase velocity bias in ambient noise tomography, with application to SE Tibet, *Geophys. J. Int.*, **179**(2), 1113–1132.

SUPPORTING INFORMATION

Supplementary data are available at *GJI* online.

Figure S1. Same as Fig. 3 in the main text, but for ‘xRL’ source excitation.

Figure S2. Same as Fig. 5 in the main text, but for ‘xRL’ source excitation.

Figure S3. HVR sensitivity as a function of depth. Similar to Fig. 4 but for a uniform source distribution and model perturbations applied at different depths as indicated on the left—all layers (same as Fig. 4) in the top row, followed by layer-wise perturbation in each successive row. Note that the last ‘layer’ is the half-space underlying the model.

Figure S4. Same as Fig. S3 but for $f_0 = 0.75$ Hz, period ~ 13.33 s.

Figure S5. Same as Fig. S3 but for $f_0 = 0.05$ Hz, period 20 s.

Please note: Oxford University Press is not responsible for the content or functionality of any supporting materials supplied by the authors. Any queries (other than missing material) should be directed to the corresponding author for the paper.

APPENDIX A: MODEL M_0

The model is shown in Table A1 and its surface wave eigensolutions are plotted in Figs A1 and A2.

Table A1. The crustal model.

Depth (km)	V_P (km s ⁻¹)	V_S (km s ⁻¹)	ρ (g cm ⁻³)
0.00	6.200	3.600	2.800
17.00	6.600	3.700	2.900
34.00	7.300	4.000	3.100
50.00	8.200	4.700	3.400

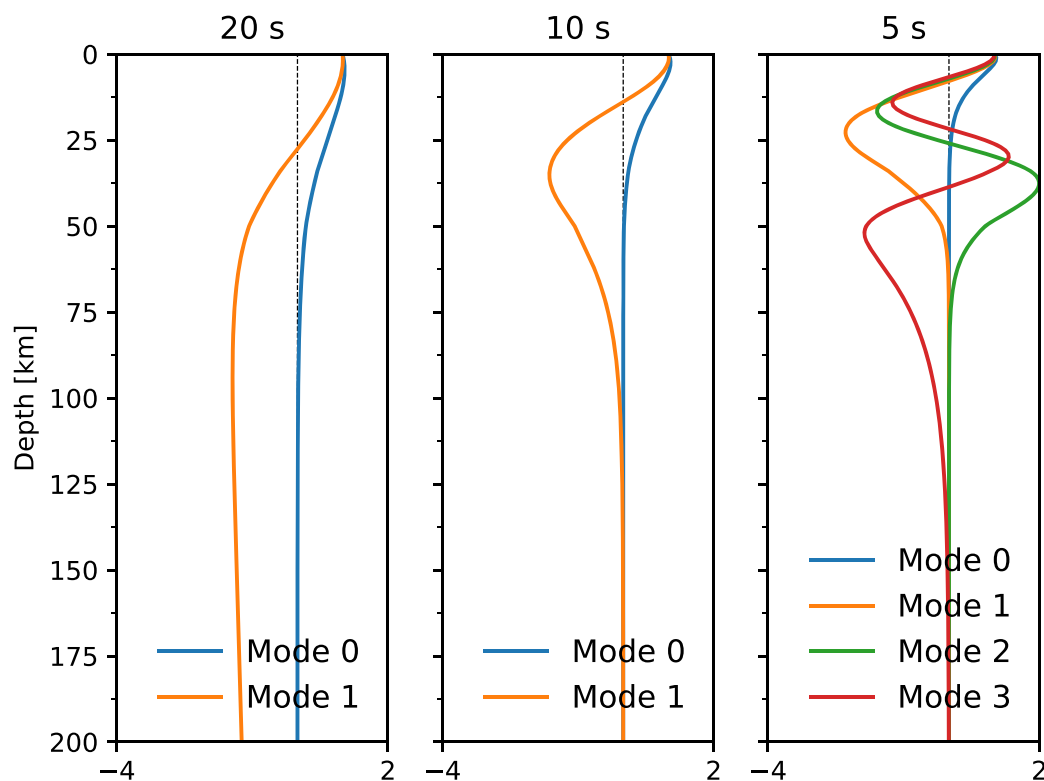


Figure A1. Rayleigh-wave vertical displacement eigenfunctions (normalized to unit surface displacement) for the fundamental and higher modes in model M_0 , at three different periods indicated at the top. Note that most results in this paper are presented at 10 s period.

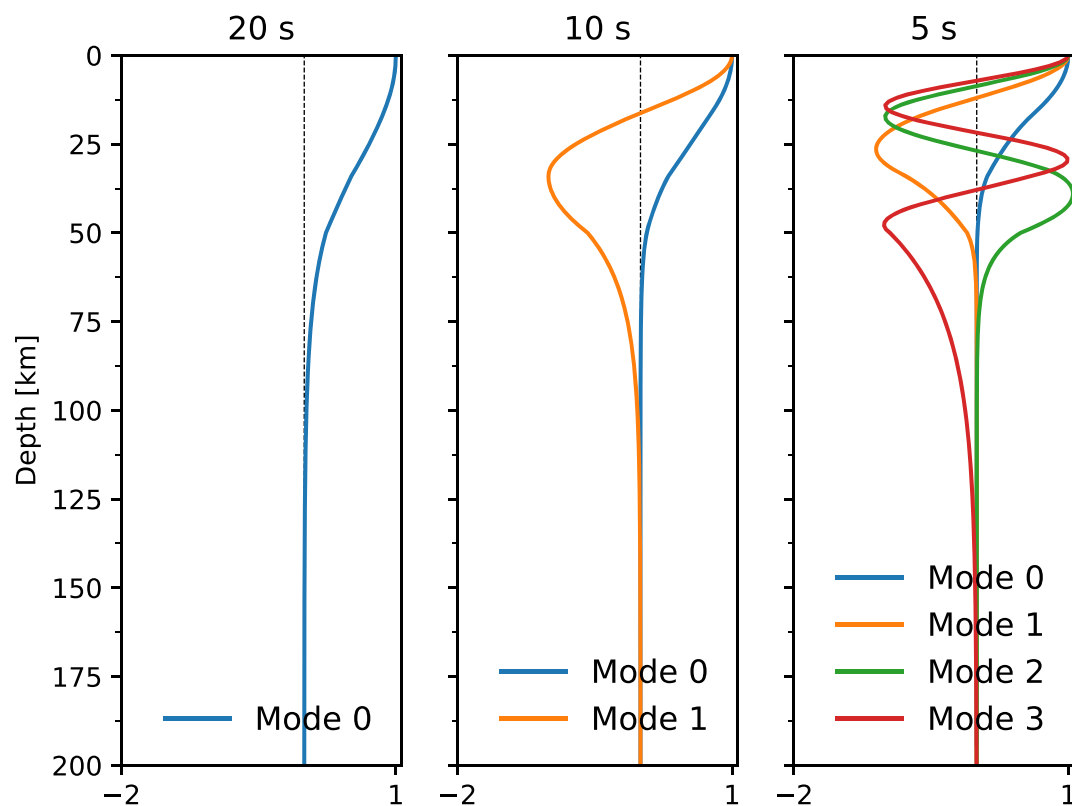


Figure A2. Love-wave displacement eigenfunctions (normalized to unit surface displacement) for the fundamental and higher modes in model M_0 , at three different periods as in Fig. A1.